A surrogate-based multi-disciplinary design optimization framework modeling wing–propeller interaction

Alba, Christian; Elham, Ali; German, Brian J.; Veldhuis, Leo L.L.M.

DOI
10.1016/j.ast.2018.05.002

Publication date
2018

Document Version
Final published version

Published in
Aerospace Science and Technology

Citation (APA)
Alba, C., Elham, A., German, B. J., & Veldhuis, L. L. L. M. (2018). A surrogate-based multi-disciplinary design optimization framework modeling wing–propeller interaction. *Aerospace Science and Technology*, *78*, 721-733. https://doi.org/10.1016/j.ast.2018.05.002

Aerospace Science and Technology 78 (2018) 721–733

Contents lists available at ScienceDirect

Aerospace Science and Technology

www.elsevier.com/locate/aescte

A surrogate-based multi-disciplinary design optimization framework modeling wing–propeller interaction ☆

Christian Alba [a], Ali Elham [b,*], Brian J. German [c], Leo L.L.M. Veldhuis [a]

[a] Delft University of Technology, 2629 HS Delft, the Netherlands
[b] Technische Universität Braunschweig, 38108 Braunschweig, Germany
[c] Georgia Institute of Technology, Atlanta, GA, 30332, USA

ARTICLE INFO

Article history:
Received 13 February 2018
Received in revised form 16 April 2018
Accepted 2 May 2018
Available online 9 May 2018

Keywords:
Wing–propeller interaction
Multidisciplinary design optimization
Surrogate modeling

ABSTRACT

This paper presents a multi-disciplinary design optimization (MDO) framework for design of a general aviation aircraft wing considering the effects of tractor propellers on the wing aerodynamic characteristics. In pursuit of this objective, a wing–propeller full-interaction aerodynamic routine was developed and integrated with structural and performance models. A substantive contribution of the work is the approach for effectively modeling wing effects on propeller slipstream development while still leveraging traditional propeller and wing analysis tools. Several optimizations were carried out, starting from an existing aircraft design, to test different local and global surrogate-based optimization frameworks and to allow for the assessment of the resulting solutions and corresponding computational performance metrics. Examination of the total function calls and run times showed that the use of surrogate models improves overall optimization performance, provided that suitable surrogate modeling techniques are chosen.

1. Introduction

The history of propeller powered aircraft began in parallel with aviation itself via the first flight of the Wright Flyer in 1903. More than a century later, propellers have not lost their appeal, and although facing competition from turbofans in certain market segments, they still constitute the predominant means of propulsion for small general aviation aircraft. Moreover, the advances in electric propulsion achieved over the past decade have opened a wide range of design opportunities, stemming from the higher scalability and flexibility of electric motor configurations when compared to piston or turboprop engines. In this context, *distributed electric propulsion* based on multiple propellers has become a cornerstone technology in NASA's research into new concepts for air mobility [1].

Generally speaking, wings and propellers have historically been designed and optimized independently. However, when a wing design and a propeller design are combined in a tractor configuration, a complex system of aerodynamic interaction effects develops, and the individually optimized designs become sub-optimal from the standpoint of system level performance.

The most recognizable wing–propeller interaction effects are those induced by the propeller on the wing and can be modeled in relatively simple ways by superimposing an isolated propeller flow field on a wing flow field with an appropriate linear aerodynamics model. These effects include an increase in dynamic pressure over the portion of the wing blown by the propeller—mainly related to slipstream axial induced velocities—and a wing local angle of attack variation—mainly related to slipstream tangential induced velocities. Both effects alter the wing lift distribution as shown in Fig. 1 from Veldhuis [2].

Several additional interaction effects induced by the propeller on the wing are also present but require more sophisticated models to predict. These effects include the contraction of the propeller slipstream, which further affects the trailing wing lift distribution and increases viscous drag, and the higher turbulence levels characterizing the field of propeller induced velocities, which promote wing boundary layer transition [3] and result in an additional increase in viscous drag.

If the effects of the wing on the upstream propeller are also considered, a *full interaction* [4] aerodynamics analysis is required. A full interaction model can capture the field of induced velocities generated by the lifting wing that alters the angle of attack per-

☆ This paper has been modified from Alba, C. Elham, A., German, B., Veldhuis, L.L.M., A Surrogate-Based Multi-Disciplinary Design Optimization Framework Exploiting Wing–Propeller Interaction, AIAA Aviation 2017, June 2017, Denver, Colorado, USA.

* Corresponding author.
E-mail address: a.elham@tu-braunschweig.de (A. Elham).

https://doi.org/10.1016/j.ast.2018.05.002
1270-9638/

Nomenclature

C_N	propeller normal force	V_r	propeller radial induced velocity
D	propeller diameter	V_∞	freestream velocity
J	propeller advanced ratio	α_p	propeller angle of attack
R	propeller radius	β_0	blade pitch angle
T	propeller thrust	θ_s	propeller streamtube axis deflection angle
V_x	propeller axial induced velocity	σ_e	effective blade solidity

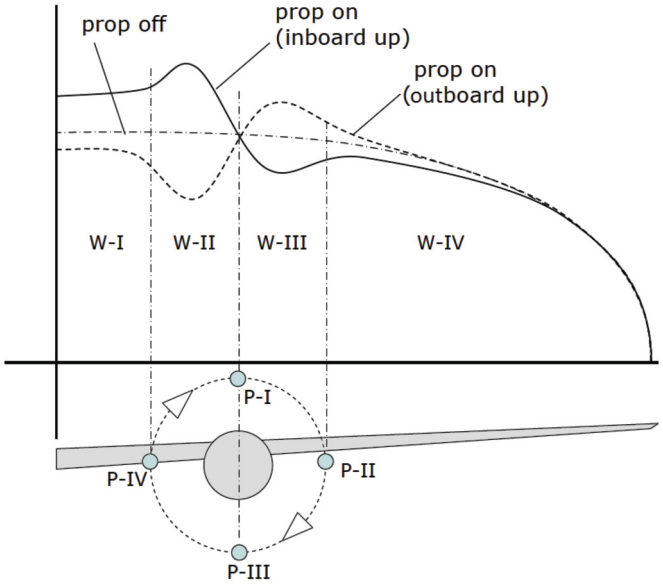

Fig. 1. Wing lift distribution alteration induced by a tractor propeller [4].

ceived by the propeller and its slipstream, resulting in a vertical force on the propeller plane (*hub lift* as defined by Witkowski [5]) and the deflection of the shed slipstream tube. Additionally, a wing following a tractor propeller acts like a stator vane, recovering part of the swirl present in the slipstream. This deforms the slipstream itself, having consequences on propeller performance and on the local flow at different chord-wise stations along the wing itself.

Some authors in the past have developed aerodynamic tools that model certain interaction effects between propellers and wings. Among these are Witkowski [5], Cho and Cho [6], Ferraro et al. [7], Patterson et al. [9,8], and Veldhuis [4]. These prior works have focused primarily on characterizing aspects of the aerodynamic interaction or in modeling aggregate system performance.

The goal of the present work is to examine the fuel savings opportunities associated with well-integrated propeller and wing designs by developing a multi-disciplinary design optimization (MDO) framework with fully-coupled wing–propeller interaction. The application area of interest is to optimize the wing design of general aviation aircraft with tractor-configuration wing-mounted propellers. Achieving these objectives required building appropriate aerodynamic models and coupling tools to perform a full-interaction analysis and integrating the tools into a suitable optimization architecture enhanced by surrogate models to reduce solution time.

The paper is organized as follows. Section 2 elaborates on the development, capabilities, and limitations of the analysis tools necessary to fulfill the research objective. These tools include models for isolated propeller and wing aerodynamics, interaction models for coupling propeller and wing aerodynamics, and a model for fuel consumption in an aircraft mission. Section 3 presents the complete optimization problem statement, and Section 4 introduces the surrogate models and the surrogate-based optimization framework. Finally, Section 5 reports the results of the different optimizations conducted, including comments on the optimal designs and the observed trends, as well as the numerical performance of each implemented framework.

2. Multi-disciplinary analysis framework

In this section, we describe the multi-disciplinary analysis (MDA) framework. The core of the MDA is the full-interaction propeller and wing aerodynamics routine, consisting of several constituent models. Additionally, an aircraft performance model and a wing weight assessment model are incorporated to provide a system-level assessment of fuel burn associated with changes to the wing design.

The following specific models are included as constituent elements in the MDA:

- Propeller isolated aerodynamics model, including slipstream development effects
- Wing isolated aerodynamics model
- Full-interaction aerodynamic coupling model
- Wing weight assessment model
- Aircraft performance model

In this research the wing and propeller are modeled separately and a novel method is developed to couple their effects. Such an approach was chosen based on the desire for a low to mid fidelity approach that is also appropriate for the degree of geometric fidelity of propeller and wing designs, which is typically available in conceptual and early preliminary design studies. These considerations motivated us to exclude unsteady or time averaged CFD and fully coupled unsteady free wake wing and propeller panel codes because of both solution time and the degree of geometric definition that is required to achieve adequate solution fidelity. Our viewpoint is that this approach could be used to develop good initial propeller and wing designs, considering aerodynamic coupling, that can then be used as the basis for more detailed CAD lofting and subsequent coupled analysis in CFD or similar tools.

2.1. Propeller isolated aerodynamics model

XROTOR was selected as the basis for isolated propeller aerodynamics modeling [10]. For a given propeller design, XROTOR has the capability to predict axi-symmetric and spatially non-uniform distributions of slipstream induced velocities and to estimate relationships between thrust and power required. The code models blade geometry in terms of radial distributions of chord, twist, and airfoil shape and incorporates models of airfoil viscous losses. One analysis mode of XROTOR is built as an extension of Goldstein's solution [11] to an arbitrary number of blades and arbitrary radial load distributions.

Despite its wide range of capabilities for both analysis and design of propellers, XROTOR provides values for induced velocities only at the propeller plane and in the far field and does not provide solutions for slipstream contraction and radial flow. Additionally, XROTOR only models inflows parallel to the propeller axis.

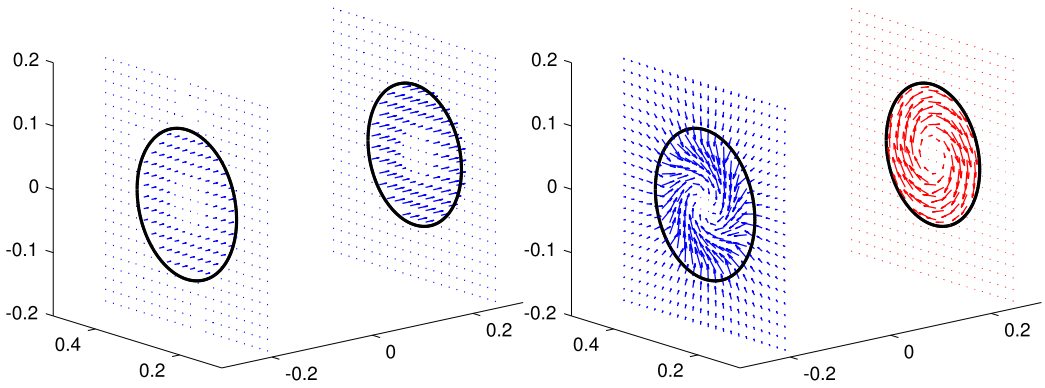

Fig. 2. Slipstream induced velocities: axial (left) and in plane (right).

To account for slipstream development and contraction, we leveraged a vortex-theory-based procedure formulated by Conway [12] to provide capabilities for evaluating induced velocities of an isolated propeller anywhere in the flow field. Conway's simplest formulation, which assumes an elliptic distribution of induced velocities, was adopted with the presumption that the predicted streamtube contraction is generally indicative for other propeller radial loadings. This model consists of the following set of equations, with $V_x(r,x)$ and $V_r(r,x)$ representing the axial and radial induced velocity at the (r,x) spatial coordinates. r is a radial coordinate, assuming a value of zero at the slipstream axis, and x is the axial coordinate, assuming a value of zero at the propeller plane. V_x is defined to be positive in the downstream direction, while V_r is positive in positive radial direction.

$$V_x(r,0) = \frac{V_{x_0}}{R}\sqrt{R^2 - r^2} \tag{1}$$

$$V_r(r,x) = \frac{V_{x_0}|x|}{2r}\left(\frac{1}{a} - a\right) - \frac{V_{x_0} r}{2R}\arcsin\left[\frac{2R}{\sqrt{x^2+(R+r)^2}+\sqrt{x^2+(R-r)^2}}\right] \tag{2}$$

$$V_x(r,x) = 2V_x(r,0) + V_{x_0}\left\{-a + \frac{x}{R}\arcsin\left[\frac{2R}{\sqrt{x^2+(R+r)^2}+\sqrt{x^2+(R-r)^2}}\right]\right\} \tag{3}$$

$$a = \sqrt{\frac{\sqrt{(R^2-r^2-x^2)^2+4R^2x^2}+R^2-r^2-x^2}{2R^2}} \tag{4}$$

To leverage the model for predicting streamtube contraction, we scaled the Conway distribution by the velocities at the propeller plane to determine a set of coefficients that could be multiplied by the propeller plane velocities predicted by XROTOR for arbitrary propeller designs. The resulting model represents an approximation for the complete 3D induced velocity vector at any point in space downstream of the propeller plane. This formulation also allows for the identification of the streamtube boundaries.

Fig. 2 shows a qualitative example of the results of this approach in modeling the induced velocity field of a 0.236 m diameter propeller. The figure on the left presents grids of axial induced velocity vectors at the propeller plane (on the left) and at a location downstream (on the right). The increase in axial velocity for points farther away from the propeller plane is clearly noticeable. The figure on the right presents tangential and radial induced velocities, illustrating the generally greater magnitude of radial flow within the slipstream, as well as the extension of radial flow to the region outside of the slipstream.

In addition to the downstream distribution of induced velocities, XROTOR also does not model propellers at angle of attack with respect to the incoming flow. A momentum-based semi-empirical procedure described by De Young [13] was therefore adopted to provide an estimate of these effects. Specifically, De Young's model estimates sensitivities of propeller normal force and streamtube axis deflection angle with respect to propeller angle of attack, i.e. $\frac{dC_N}{d\alpha_p}$ and $\frac{d\theta_S}{d\alpha_p}$, respectively.

De Young's method, described in Equations (5) through (10), is an extension of the momentum-theory-based approach presented by Ribner [14], [15] to higher angles of attack and arbitrary blade shapes. The method achieves higher accuracy because of its greater flexibility and the incorporation of empirical coefficients based on propeller wind tunnel tests.

$$\frac{dC_N}{d\alpha_p} = \frac{4.25\sigma_e}{1+2\sigma_e}\cdot\sin(\beta_0+3)\cdot f\cdot\frac{\pi J^2}{8} \tag{5}$$

$$\sigma_e = \frac{4B}{3\pi}\cdot\frac{c_{av}}{2R}\cdot\frac{Cl_{\alpha_{av}}}{0.95\cdot 2\pi} \tag{6}$$

$$f = 1 + 0.5\cdot[\sqrt{1+T_C}-1] + \frac{T_C}{4(2+T_C)} \tag{7}$$

$$T_C = \frac{8}{\pi J^2}\cdot\frac{T}{\rho n^2 D^4} \tag{8}$$

$$J = \frac{V_\infty}{n D} \tag{9}$$

$$\frac{d\theta_S}{d\alpha_p} = \frac{1+T_C-\sqrt{1+T_C}}{2+T_C} + \frac{3+2T_C+\sqrt{1+T_C}}{(2+T_C)^2}\cdot\frac{\sqrt{1+T_C}}{4}\cdot\left.\frac{dC_N}{d\alpha_p}\right|_{T_C=0}\cdot\frac{8}{\pi J^2} \tag{10}$$

In the formulation, σ_e represents the so-called effective blade solidity, β_0 is the blade pitch angle referred to the zero-lift line of the 75% R airfoil section, T is the propeller thrust, D is the propeller diameter, V_∞ is the freestream velocity, and n is the propeller rotational speed in rotations per second. J is the propeller advance ratio, c_{av} is the average blade chord from $0.2R$ to R, and $Cl_{\alpha_{av}}$ is the average blade lift curve slope.

2.2. Wing isolated aerodynamics model

The aerodynamics of the isolated wing is modeled by an approach leveraging the vortex lattice method (VLM) and strip theory [16]. The core of the VLM code Tornado [17] was selected as

a starting point. Several modifications were applied to the original version, including an improved camber line estimation function, a faster and more accurate trim function based on a Newton–Raphson scheme, and an assessment of the quarter chord twist moment distribution.

A slightly modified version of the quasi-3D code developed by Mariens, Elham and Van Tooren [18] was adopted to model wing viscous drag. The approach is based on the assumption that for zero to low sweep wings, overall viscous drag can be estimated by integrating airfoil drag data. Starting from a spanwise lift distribution calculated with VLM or similar tools, an airfoil viscous analysis tool can be run at a limited set of spanwise stations at the given local lift coefficients. The routine is run iteratively to converge to estimate the section drag at each span station at the appropriate effective local angle of attack. The resulting section drag predictions are integrated to estimate the viscous drag of the entire wing. In this research, XFOIL [19] was chosen for the 2D airfoil viscous drag prediction.

2.3. Full-interaction aerodynamic analysis

Several steps were required to combine the isolated propeller and wing modeling tools to capture the relevant interaction effects. The first step was to include propeller slipstream effects on wing aerodynamics. This was achieved by modifying the wing analysis code in three ways:

1. Enforcement of the non-penetration condition: The combined XROTOR–Conway–De Young capability of predicting slipstream induced velocities at any point in space was leveraged by adding propeller induced velocities to the freestream at all of the wing VLM lattice control points and enforcing non-penetration of the combined velocity.
2. Computation of forces from bound vortices through the vector form of the Kutta–Joukowski equation: The component of slipstream induced velocities *normal* to the freestream direction was added to the freestream vector. This reflects a typical approach adopted in simpler codes when accounting for wing downwash in induced drag calculations and prevents an incorrect scaling of forces which would entail an overestimation of the wing lift distribution.
3. Flow conditions for strip analysis: The component of slipstream induced velocities *parallel* to the freestream direction was added to the freestream vector. This approach allows our Q3D model (which interpolates the VLM predicted lift distribution) to converge to the appropriate local effective angles of attack and to expose each section to the right Mach and Reynolds numbers. Scrubbing drag related to increased dynamic pressure is also automatically accounted for with this approach.

The modifications described above complete the *one-way* interaction portion of the tool. However a *full interaction* analysis requires at least the inclusion of the most relevant wing effects on propellers as well. In this context, studies in the past have demonstrated that the relevance of certain effects on overall aerodynamics often depend on the working conditions of the compound system (wing lift coefficient, propeller advance ratio) and on the relative dimensions of the two elements [20]. The decisions made based on relevance of effects in the present work were based on the applicability of the resulting tools to typical general aviation aircraft (often featuring propellers of a diameter similar to the wing chord in cruise flight, thus with moderately loaded propellers). In similar conditions, authors including Witkowski [5] and Samuelsson [21] noticed that wing effects on the propeller aerodynamics generally have a negligible effect on propeller performance metrics such as thrust and power.

However, the following three full interaction effects were viewed as non-negligible and therefore modeled in the present work:

- Appearance of a propeller normal force
- Deflection of the propeller streamtube
- Reduction in slipstream swirl

To model propeller normal force, the procedure suggested by De Young [13] and discussed in Section 2.1 was applied by adopting an equivalent propeller incidence determined by the freestream flow (α_p) and the wing up-wash (w). Eq. (11) gives the propeller normal force coefficient (C_N) based on this equivalent incidence.

$$C_N = \frac{dC_N}{d\alpha_p} \cdot \left[\alpha_p + \arctan\left(\frac{w}{V_\infty} \right) \right] \tag{11}$$

To model streamtube deflection, an innovative approach based on an iterative routine was adopted. Initially, the propeller incidence with respect to the freestream α_p is used to estimate the isolated propeller's streamtube deflection θ_{S_i} through the De Young procedure, as indicated in Eq. (12).

$$\theta_{S_i} = \frac{d\theta_S}{d\alpha_p} \cdot \alpha_p \tag{12}$$

Subsequently, considering that the propeller slipstream is exposed both to up-wash and down-wash while flowing over a lifting surface, a two-segment linear model for the streamtube axis is adopted. The first segment, departing from the propeller hub, is assigned an incidence θ_{S_1} with respect to the freestream and is connected with the second segment at a downstream station corresponding to the wing quarter chord. The second segment is assigned an incidence θ_{S_2}.

Superposition is used to determine the appropriate values of θ_{S_1} and θ_{S_2} by summing wing up-wash and down-wash angles to give the value of the isolated streamtube deflection, as indicated in Eqs. (13) and (14).

$$\theta_{S_1} = \theta_{S_i} + \arctan\left(\frac{\bar{w}_1}{V_\infty} \right) \tag{13}$$

$$\theta_{S_2} = \theta_{S_i} + \arctan\left(\frac{\bar{w}_2}{V_\infty} \right) \tag{14}$$

Here, $\bar{w}_1$ and $\bar{w}_2$ represent the wing wash that the first and second segments are exposed to, respectively, and are evaluated by averaging the values obtained by surveying the wing induced flow field at several stations.

The influence of wing wash on streamtube deflection and the influence of streamtube deflection on wing aerodynamics and wing wash required the described approach to be implemented in an iterative procedure converging to the appropriate θ_{S_1} and θ_{S_2} values. The procedure is schematically represented in the flowchart shown in Fig. 3. As indicated in the figure, once the streamtube axis deflection is determined, the induced velocities predicted by the Conway model were updated by referencing them to the newly defined streamtube axes.

Fig. 4, surveying the same planes as Fig. 2, shows the streamtube deflection model applied to a wing–propeller system placed at incidence. The two-segment streamtube axis is clearly visible.

It must certainly be expected that the non-smooth variation in streamtube axis angle in this model introduces small errors, as does neglecting flow distortion. Nevertheless, the approach was

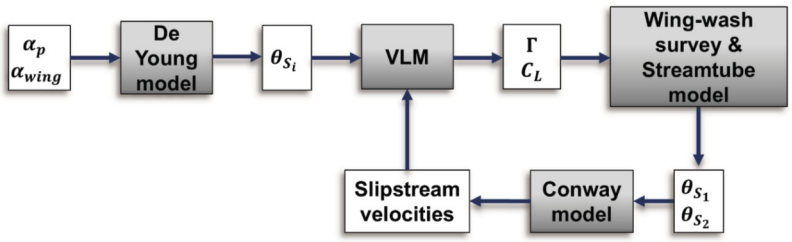

Fig. 3. Streamtube deflection model flowchart.

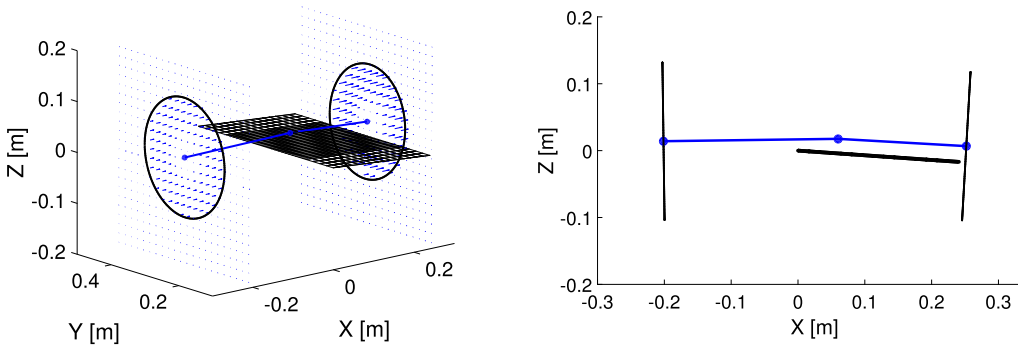

Fig. 4. Streamtube deflection influenced by wing presence: three quarter view (left) and side view (right).

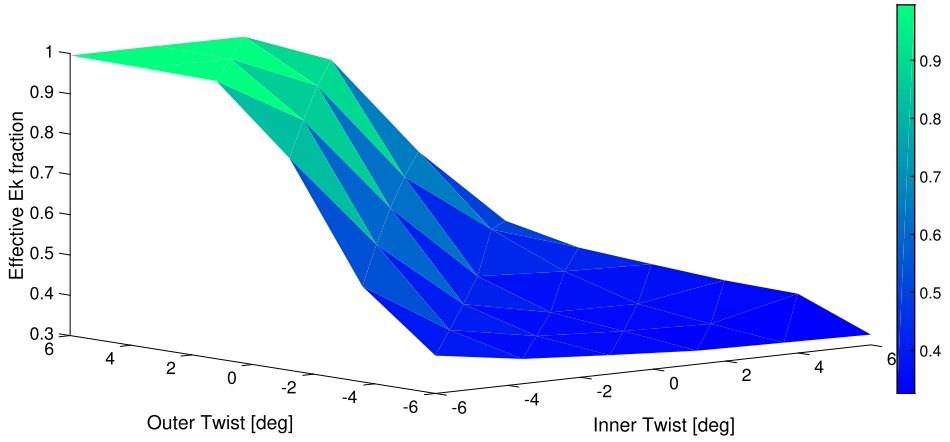

Fig. 5. Swirl recovery factor variation with wing twist distribution. (For interpretation of the references to color in this figure, the reader is referred to the web version of this article.)

demonstrated to dramatically improve the accuracy of the model in comparison to a *one-way interaction* analysis that neglects the wing induced effects on the slipstream, as shown is in the validation case presented in Section 2.4.

Another innovative analysis routine was developed to account for the swirl recovery effect. Superimposing the entire propeller swirl—as predicted by the isolated propeller aerodynamics model—with results from the wing VLM code would be physically incorrect: the wing stator vane effect alters the slipstream velocity field that the wing itself perceives. For example, Veldhuis [4] noted the need for halving propeller tangential velocities before imposing them on a trailing wing in order to properly match experimental results. He proposed a constant reduction factor of 0.5. However this approach is insensitive to wing geometry and operating conditions and represents a limitation in the present work, especially in the context of an optimization routine designed to best take advantage of propeller slipstream effects in wing design. For this reason, an active routine was developed to compute an appropriate scaling factor for each configuration and flow condition.

This routine is constructed as follows. First, a flow survey procedure is used to compute the kinetic rotational energy ($E_{K_{rot}}$) present within the streamtube boundaries due to the combination of propeller and wing induced velocities. This flow survey is carried out at several stations from propeller plane to wing trailing edge. This procedure makes it possible to determine the fraction of the isolated propeller $E_{K_{rot}}$ remaining at each station. All the recorded values are averaged, resulting in a unique aggregate measure representing the fraction of kinetic rotational energy the wing effectively perceives. The squared root of this aggregate measure was adopted as a scaling factor to be applied to the propeller tangential induced velocities before superimposing them in the wing tool in the subsequent iteration. The routine thus consists of two steps: first, performing a swirl recovery analysis, and second, imposing the scaled values of the swirl velocities on the wing analysis.

To provide a visual representation of the swirl recovery phenomenon and its effects, Fig. 5 shows the effective $E_{K_{rot}}$ fraction perceived by the wing as predicted by the described approach for different wing twist distributions. In particular, two wing sections

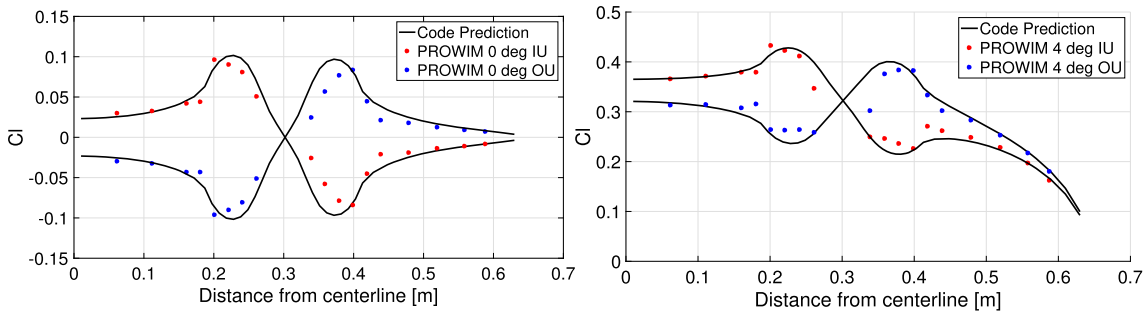

Fig. 6. PROWIM local lift coefficient distribution: 0 deg incidence (left) and 4 deg incidence (right).

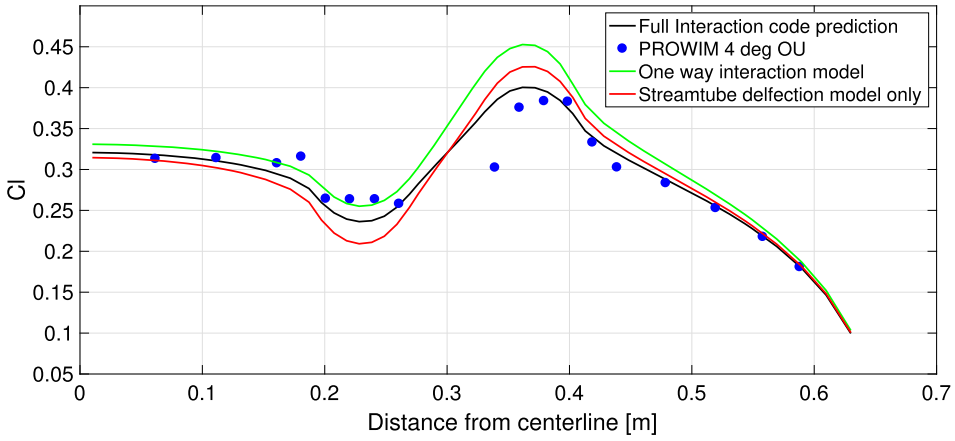

Fig. 7. One way vs full interaction model.

placed one radius inboard and one radius outboard of the propeller axis, respectively, were twisted from −6 to +6 degrees. The propeller axis, constructively locked to the wing twist, always assumed an incidence equal to the mean value of the twists of the two sections.

This example clearly reflects physically predictable trends: when the wing sections are more aligned with the incoming propeller flow, as happens when the inner twist is negative and the outer is positive (the propeller features inboard-up rotation) the swirl recovery occurs to a much lesser extent. On the other hand, when opposite wing twist distributions are employed, the field of velocities induced by the wing greatly counteracts the incoming swirl, dampening it by up to 70%.

2.4. Aerodynamics routine validation

The complete wing–propeller integration analysis model was validated against results of the PROWIM wind tunnel campaign carried out by Veldhuis [4]. The PROWIM wind tunnel model featured a straight uncambered wing blown by a tractor propeller. The propeller featured zero constructive incidence with respect to the wing.

The validation was run with 43 spanwise and 15 chordwise VLM panels and an 18 section strip analysis for viscous drag prediction. These grid densities were determined through a grid convergence study, and the span-wise spacing in the blown portion of the wing was always set equal to half that of the spacing in the unblown portions of the wing.

Fig. 6 reports the lift predictions compared to experimental data for the 0 deg and 4 deg incidence cases. Both inboard up and outboard up rotation ("IU" and "OU" in the labels) cases are presented. The code can be seen to approximate the lift distribution very well, with a minor inaccuracy visible in the region closer to the propeller hub. This inaccuracy is explained by the presence of a nacelle in the PROWIM wing, which was not modeled in our computational approach.

Further evidence of the successful implementation of the *full interaction* analysis in the present work through the development of the streamtube deflection model and the swirl recovery model can be seen in Fig. 7. This figure shows the predicted lift distribution obtained with the full-interaction model (solid line) along with the results obtained by neglecting wing influence on the streamtube development and the results obtained by including wing effects on streamtube deflection but not on swirl recovery. The results are presented for the 4 deg incidence outboard-up rotation case. The improvement in prediction accuracy of the full interaction model is striking.

Despite the lack of experimental drag data, we note how our method reflects the underlying phenomena affecting both profile and induced drag. By examining Fig. 8 for instance, representing the 4 deg incidence OU case, scrubbing drag effects can indeed be noted as a local increase in profile drag coefficient in the slipstream blown portion of the wing. From an induced drag perspective, a dramatic reduction in induced drag coefficient is achieved in the wing portion trailing the up-going blade side of the propeller. The induced drag value even becomes even negative in certain regions, indicating a net thrust contribution. This behavior confirms the studies of [4], [22], [5] and others which state that the locally increased angle of attack causes the lift vector not only to increase in magnitude but also to tilt forward.

2.5. Other models in the multi-disciplinary analysis

The aerodynamic tools described above allow for the evaluation of overall lift (wing + propeller), drag, thrust, and power for par-

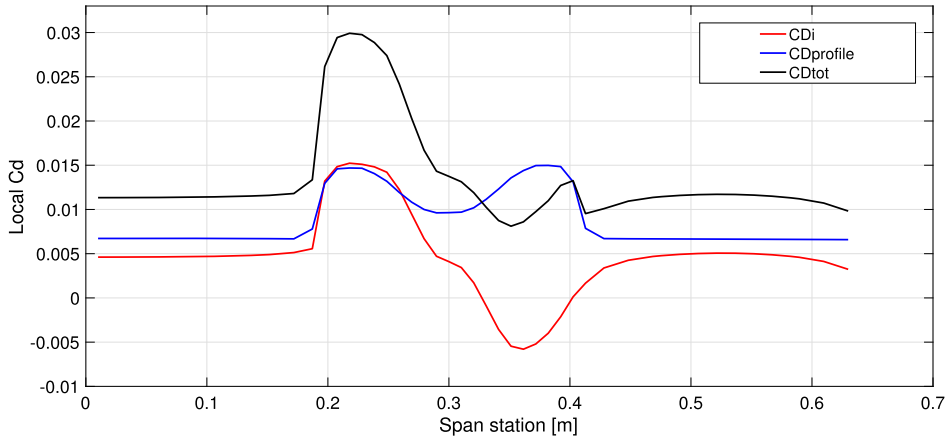

Fig. 8. PROWIM local drag coefficient distribution.

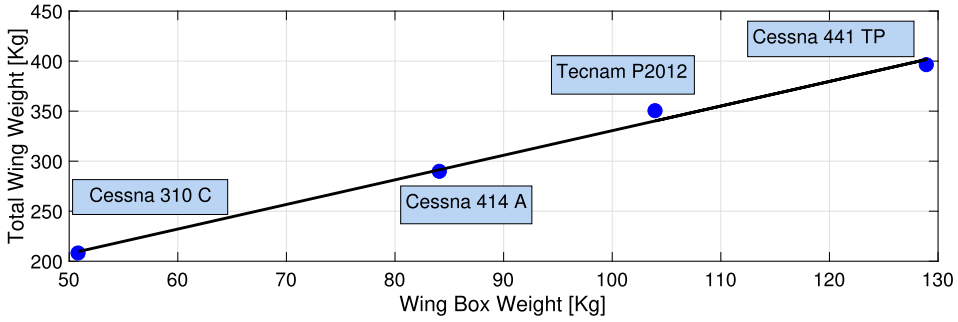

Fig. 9. Wing total weight vs wing-box weight regression for EMWET.

ticular wing and propeller designs. To evaluate fuel burn at cruise for an aircraft with a given propeller and wing design, the following additional routines were implemented:

- A performance routine, making use of the Breguet range equation to compute cruise fuel consumption.
- A trimming routine, based on the aircraft cruise weight, that computes the consequent total drag. A fixed drag term was adopted in order to account for all the non-wing contributions (fuselage, tail, and other drag sources).
- A wing weight route to estimate the weight effects of changes in the wing planform and airfoil design parameters that occur during the multi-disciplinary optimization.
- A weight routine, computing Maximum Take-off Weight (MTOW) and cruise aircraft weight. The fuel fraction method was adopted in this context, and MTOW was computed as the sum of fuel weight, wing weight and a fixed term accounting for all the non-wing contributions (payload and fuselage weights among others).

The wing weight routine is particularly important because of its close coupling with the wing design parameters and aerodynamic loads. The EMWET structural model, a class II and 1/2 tool developed by Elham et al. [23] was deemed the most appropriate tool for this purpose. It is based on strength analysis of wing box structures augmented with empirical relationships. In its underlying procedure, the weight of the most relevant elements of the wing primary structure, such as spar webs and equivalent panels, is estimated analytically according to optimum structure sizing. Span-wise lift and twisting moment distributions are obtained from the VLM code run at a critical condition dependent on the specific aircraft's V–n diagram. Subsequently, the required thickness of structural components is determined by referring to known material properties, which also allow for the evaluation of weight. The aggregate weight of all the remaining elements is computed empirically via statistical regression based on the obtained analytic results. The code accounts only for static load conditions, thus assuming that critical sizing loads are not related to aeroelastic effects.

The original formulation of EMWET was calibrated for accuracy for large commercial airliners. Modifications were required both in the analytic wing box sizing, originally complying with CS-25 regulations and thus requiring the generation of new V–n diagrams for CS-23, and in the regression coefficients adopted, which were estimated from a customized database of GA aircraft developed as part of this research. Fig. 9 shows the linear regression obtained for a few general aviation aircraft whose coefficients are reported in Eq. (15).

$$W_{wing} = 84.6108 + 2.4589 \cdot W_{wingbox} \tag{15}$$

Fig. 10 presents the design structure matrix combining all the disciplinary analyses described and indicates the three nested loops required to converge to the correct streamtube deflection angle, aircraft angle of attack, and propeller pitch and thrust.

3. Optimization problem

Having developed the full multidisciplinary analysis model, the next step to be performed in pursuit of the research objective is its integration in an MDO framework capable of discovering improved designs. The optimization problem for this work is formulated as follows:

	Air properties Prop Geometry	Air properties Range Engine specs	Air properties Wing Geometry	Extra Weight	Air properties	Air properties Geometry	Air properties Geometry	Air properties Geometry Extra Drag	
	XROTOR & CONWAY	P prop			T prop	Isolated slipstream velocities			
		PERFORMANCE		W fuel cruise					
			STRUCTURE	W wing					
			MTOW W fuel tot	WEIGHT	W cruise				W fuel tot
	AoA				TRIM	AoA	AoA	AoA	
						STREAMTUBE MODEL	Slipstream velocities CL props	Slipstream velocities	
			Cl distribution Twist distribution		CL tot	Wing Wash Swirl effective	VLM	Cl distribution Cdi tot	
	D tot							Q3D	
									Obj = W fuel tot

Fig. 10. Design structure matrix for the optimization problem.

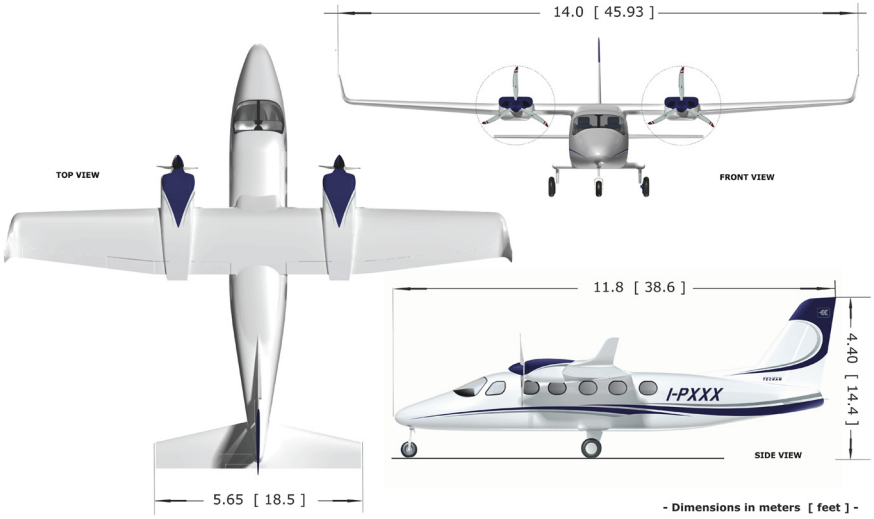

Fig. 11. Tecnam P2012 [24].

$$
\begin{aligned}
&min \quad \frac{W_{fuel}(\mathbf{x})}{W_{fuel_0}} \\
&with\ respect\ to \quad \mathbf{x} \\
&s.t. \quad \frac{MTOW/S_w}{MTOW_0/S_{w0}} - 1 \leq 0 \\
&\qquad \frac{V_{fuel}}{V_{tanks}} - 1 \leq 0 \\
&\qquad \frac{MTOW}{MTOW_0} - 1 \leq 0 \\
&\qquad x_i^l \leq x_i \leq x_i^u \qquad i = 1 \ldots 31
\end{aligned}
\tag{16}
$$

In the formulation, the objective W_{fuel} is the computed total fuel weight required for a certain design to achieve a prescribed range. The subscript 0 indicates values pertaining to the baseline design. $MTOW$ and S_w are the Maximum Take-Off Weight and wing area, respectively. V_{fuel} and V_{tanks} are the values of required and available fuel tank volume, respectively. Three inequality constraints are prescribed to prevent the baseline aircraft wing loading and MTOW from being exceeded and assuring that the predicted fuel volume fits in the wing fuel tanks. The constraint on wing loading was meant to achieve an optimal design featuring a stall speed smaller or equal to the baseline aircraft. An upper bound was set on MTOW because, although potentially achieving a reduced fuel consumption, a heavier design would entail higher costs and risks. Moreover, the analysis tool set lacked an appropriate estimation of the snowball effect of a heavier wing on other aircraft components such as landing gear, fuselage, and tail.

In order to build credibility in the analysis by comparison to an known configuration, an existing aircraft, the Tecnam P2012, was chosen as a baseline design, see Fig. 11. The Tecnam P2012 is a CS-23 to be certified twin-prop commuter aircraft, powered by two Lycoming TEO engines and capable of carrying up to nine passengers. This aircraft was chosen based on the suitability of its subsonic cruise speed to the capabilities of the aerodynamic

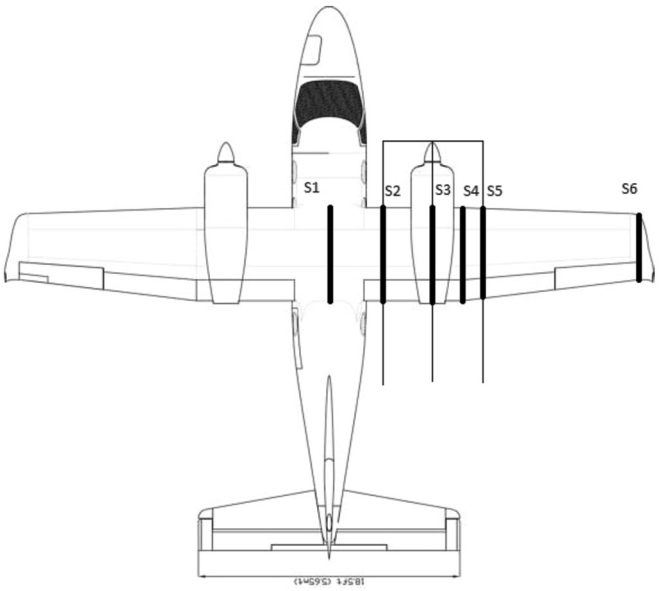

Fig. 12. Baseline aircraft sections controlled by design variables.

tools, and for the relevance of wing–propeller interaction on its overall performance. The geometry data, typical speeds, and key performance parameters were obtained from the official company website [24].

The design variables, **x**, for the optimization included the wing planform design parameters and airfoil shape parameters. The airfoils are parametrized using the Class Shape Transformation (CST) method [25]. In particular, 31 variables were defined to control the planform chord and twist distributions, the wing span, and airfoil shapes. The variables are described in the following based on Fig. 12.

- Chord of S1 (root), S4 (kink) and S6 (tip)
- Twist of S2, S5 (edges of propeller projection), and S6.
- Wing span defined as spanwise distance between S6 and S5.
- 8 CST coefficients shaping the S1 airfoil (4 CST coefficients for the upper surface and 4 CST coefficients for the lower surface)
- 8 CST coefficients shaping the S3 (engine section) airfoil
- 8 CST coefficients shaping the S6 airfoil

The propeller span-wise position was fixed to its original value, and its incidence was locked to that of the wing trailing section.

4. Surrogate models and optimization frameworks

An additional aspect of this research was the assessment of the most suitable surrogate models for improving the performance for the optimization problem stated in Section 3. Three modeling techniques were examined, namely Response Surface Models (RSM), Radial Basis Functions (RBF) and Kriging. Both the RSM and RBF procedures were coded in vectorized form and with analytic derivatives calculation in the MATLAB environment, and the open source MATLAB ooDACE toolbox by Couckuyt, Dhaene and Demeester [26] was chosen to implement the Kriging procedure.

From the optimization problem formulation in Eq. (16), it can be observed that surrogate models need to be built not only for the objective function but also for the metrics involved in the constraint functions. Surrogate models were therefore constructed for following four functions:

Table 1
Error metrics and training time for different surrogate models of normalized fuel weight obtained with the split sample approach.

	RSM	RBF	Kriging
RMSE	0.0194	0.0198	0.0077
MAX rel	0.0559	0.0624	0.0221
R^2	0.8115	0.8033	0.9701
Training time [s]	0.0098	0.0231	106.45

- $\frac{W_{fuel_{tot}}}{W_{fuel_{tot_0}}}$
- $\frac{V_{fuel}}{V_{tanks}}$
- $\frac{MTOW/S_w}{MTOW_0/S_{w_0}}$
- $\frac{MTOW}{MTOW_0}$

Before adopting any surrogate in an optimization solution procedure, one should assess the accuracy of the model via commonly accepted metrics. According to the *split sample* [27] approach, the entire sampling set of data should be split in two subgroups, namely the *training set*, upon which the surrogate is built, and the *testing set*, for which the surrogate prediction is compared with the real function values. Three metrics were adopted to measure the models accuracy, namely the *Root Mean Square Error* (RMSE), the *Maximum Absolute Error* (MAX), and the *R square value* (R^2) [28].

As an example of the implemented procedure, the following results represent a split sample performed on different $\frac{W_{fuel_{tot}}}{W_{fuel_{tot_0}}}$ surrogates. A 350 points Latin Hypercube database was chosen in line with typical suggestions for a minimum reasonable number of samples (e.g. Jones suggests at least 10 samples per variable [29]), and a 20% testing set was selected based on common practice [30]. A second order RSM, an RBF with cubic basis functions, and a Gaussian covariance function based Kriging model were compared. Table 1 reports the values of error metrics and training time for each of the three models. The training was performed on a machine featuring a 2.4 GHz processor and 8 GB of RAM.

A significant difference which can be noticed between the models is their training complexity and time. The RSM and RBF methods are based on the multiple linear regression technique in which the most computationally demanding step is the evaluation of a matrix inverse or pseudo-inverse. A complete RSM or RBF surrogate model can therefore be built in a fraction of a second. On the other hand, Kriging models are trained via a complex optimization problem to determine the values of the model's hyperparameters [31]. This training procedure can take up to several minutes. However, the predictive accuracy obtained with Kriging models even with very limited sets of training points is striking compared to the other models, as can be noted by comparing the error metrics presented in Table 1.

When applying surrogate modeling to optimization, accuracy is not the only factor to be considered. Especially when envisioning the implementation of model refinement procedures during the optimization process, training time plays a crucial role. The consideration that surrogate models for four different responses needed to be built for the present optimization problem indicated that the long training time requirement for Kriging might present a considerable limitation to its applicability for on-line refinement. The suitability of Kriging in this context was evaluated empirically in example optimization studies.

The present work adopted two different surrogate based *frameworks*, both featuring on-line model refinement, and following a routine which can be represented with the flowchart in Fig. 13. After the generation of an initial sample set with a suitable Design of Experiments (DoE) and the construction of initial surrogate models, an optimizer is run with the surrogates, resulting

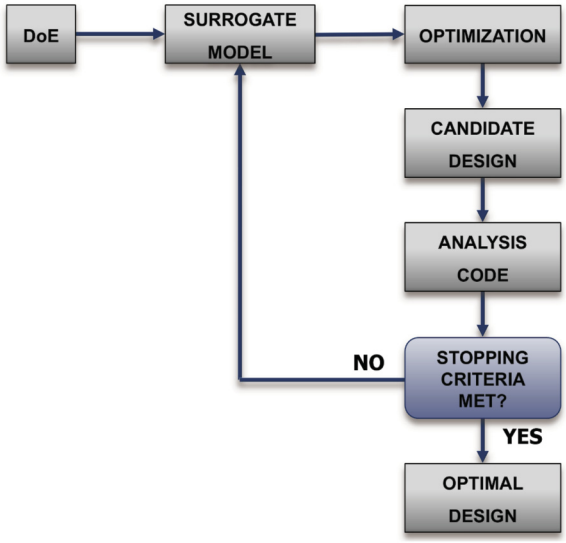

Fig. 13. Generic surrogate-based optimization framework flowchart.

in a candidate optimum with predicted objective and constraint values. The original MDA itself is subsequently run at the candidate design point, and certain metrics are assessed to determine the accuracy of the surrogate predictions and/or the performance improvement achieved. Similar metrics are adopted as stopping criteria of an iterative routine to determine whether the currently-identified design should be accepted as the estimate of the optimum or whether the response from the full MDA should instead be added to the samples set, the models updated and re-trained, and the optimization carried out again.

The first implemented framework was the *searching surrogate models* approach by Hahn and Zhang [32]. Referring to Fig. 13, this framework adopts a *local* optimization algorithm with the same objective function as the main problem statement. Such a framework provides *local* searching capabilities, due to the combined adoption of a local optimizer and the fact that surrogate refinements occur only at already promising designs—designs near which, at least according to the best available surrogates, a local minimum is present.

The second framework implemented in the present work makes it possible to perform a *global* optimization through the balancing of *exploration* and *exploitation* [27,33]. This approach is the Efficient Global Optimization (EGO) method by Jones [29], which relies on the capability of surrogate models such as Kriging to provide a measure for uncertainty at any point in the design space. At each iteration of such a framework, an unconstrained global optimization is performed in order to maximize a so-called *Expected Improvement* (EI) function. The maximization entails the simultaneous search for better–performing designs according to the present model and for points in areas of the design space where the model uncertainty is the highest. When dealing with constrained optimization problems, the expected improvement function is multiplied by an estimation of the probability of satisfaction of each constraint, under the assumption that constraints and objective are statistically uncorrelated [34]. The term *probability* is here related to the stochastic nature of models such as Kriging, which, at any point in the design space, provide a prediction of the mean value and variance of a response.

For each of the frameworks, all the optimizations run in the present work were carried out with a multi-disciplinary feasible (MDF) architecture [35], in which each iteration of the optimization problem is run on a fully *consistent* design. For all algorithms, a constraint tolerance of 10^{-4} was applied.

5. Results

Four optimizations were performed in the present work:

1. A *non*-surrogate-based optimization leveraging sequential quadratic programming (SQP) using the original MDA.
2. An RBF-based searching surrogate model, making use of the SQP optimization algorithm.
3. A Kriging-based searching surrogate model, again, making use of the SQP optimization algorithm.
4. An EGO approach, making use of a genetic algorithm (GA).

In the RBF-based optimization, the models with the best-performing basis function were selected. For the Kriging model, a Gaussian correlation function used. For the EGO approach, the same Kriging model was leveraged, and the MATLAB genetic algorithm routine was used to maximize the EI at each iteration.

The direct optimization of the MDA with SQP was viewed as the yardstick against which the other local optimizations were evaluated. All three surrogate-based optimizations were run starting with the 350 sample Latin hypercube design previously described. The two searching surrogate optimizations were carried out with the MATLAB SQP as the inner optimization algorithm and were set to stop when the relative improvement over subsequently determined feasible optima decreased below a tolerance of 10^{-4}.

When dealing with global optimizations such as the one implemented with the EGO approach, this approach to a stopping criterion cannot be applied, as subsequent designs can differ substantially. In this context, a maximum number of 200 *stall iterations*—subsequent iterations in which the optimizer failed at finding better performing feasible designs—was adopted as a stopping criterion.

The following discussion of the results refers to the data reported in Table 2, showing key performance indicators of the optimizations, and Figs. 14 through 20, showing key features of the optimal designs such as lift, drag, and pressure distributions, wing planform shapes, twist distributions, and airfoils shapes. It should be noted that the total times of the optimizations except direct SQP, include the time of generating the initial set of samples (16.04 h) plus the time of the optimization as shown in Table 2.

From Table 2, one can observe that all the described optimizations successfully found better–performing designs, resulting in total fuel savings ranging from 5.3% to 6.8%. The best performing design was found by the EGO approach, while the searching RBF yielded the lowest improvement. Despite the resulting designs being different, the trends in the results showed several similarities. In particular, all of the optima had the following features in comparison to the baseline Tecnam P2012 design:

Table 2
Summary of optimizations key performance parameters.

	Direct SQP	Search RBF	Search Kriging	EGO
Fuel savings	5.753%	5.297%	6.708%	6.818%
Total time	31.2 h	16.04 h + 3.25 h	16.04 h + 7.03 h	16.04 h + 55.41 h
Iterations	24	79	104	554
Fcn calls	884	429	454	904

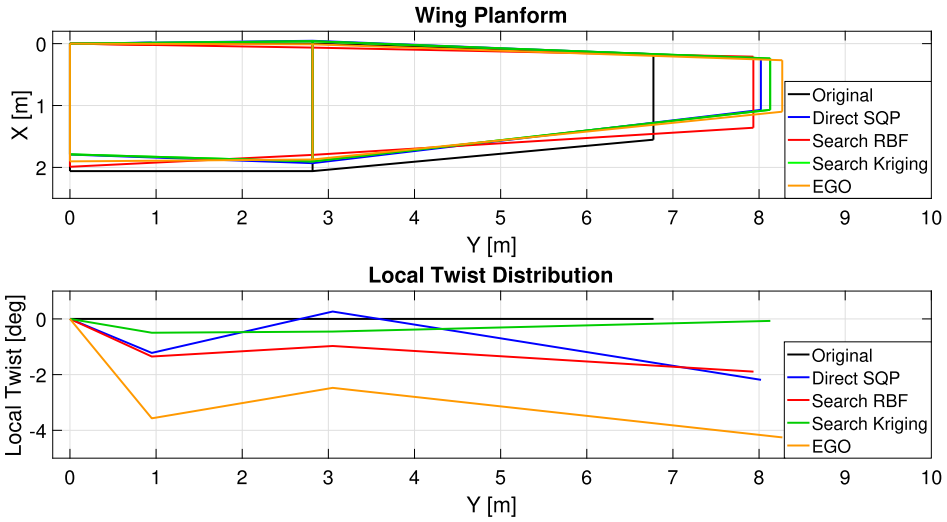

Fig. 14. Wing planform and twist distribution for baseline and optimal designs.

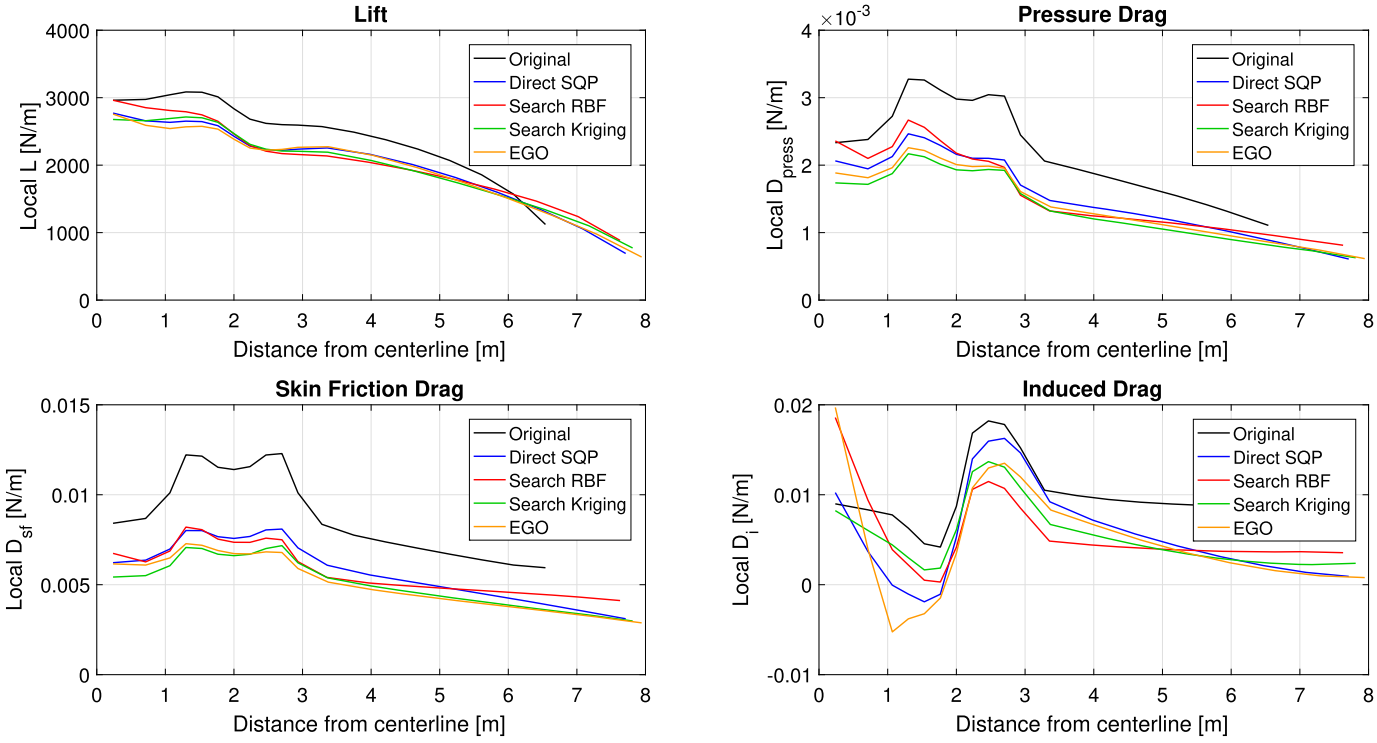

Fig. 15. Spanwise lift and drag components distributions for baseline and optimal designs.

- Higher wing span and aspect ratio, resulting in a lower span loading and thus lower induced drag (D_i in Fig. 15).
- Adjusted wing twist or airfoil camber to better align the blown sections of the wing with the incoming flow from the propeller, which allowed for a reduction in inviscid drag D_i.
- More triangular lift distribution compared to the baseline, reflecting the effect of the wing structural weight and the MTOW constraint.
- Increase in all the airfoil thickness-to-chord ratios, with the greatest increase at the wing root, to counterbalance the effect on wing weight caused by a longer span.
- Sharper leading edges and an afterward shift of the maximum thickness location for airfoils at all spanwise stations, allowing for increased laminarity and thus reduced skin-friction and pressure drag (D_{sf} and D_{press} in Fig. 15). In many cases, these effects were also achieved by introducing a negative camber (reflex) in the aft portion of profiles (see Figs. 16 through 19), to extend the favorable pressure gradient on the lower surface as far afterward as possible, as apparent in Fig. 20.
- Increase in average camber of the blown sections of the wing, reflecting findings of authors such as Veldhuis [4], who demonstrated that lower wing induced drag can be achieved when a tractor propeller is inclined downward with respect to the trailing wing. Because the propeller incidence was locked in our routine to the incidence of the wing engine section, the increase in airfoil camber reflected the natural tendency of the optimizer to mimic this downward tilting of the propeller.

6. Conclusions

The present work was motivated by the lack of past published research in the area of MDO for optimizing wing designs with

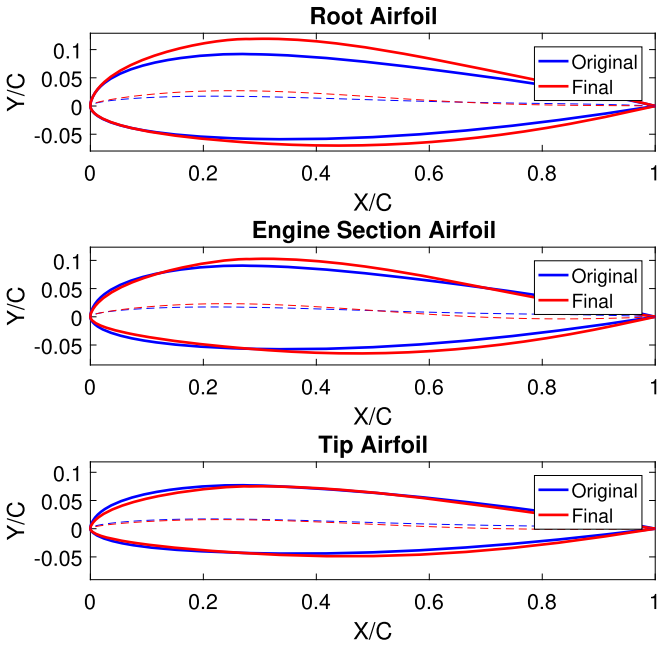

Fig. 16. Optimal airfoils direct SQP.

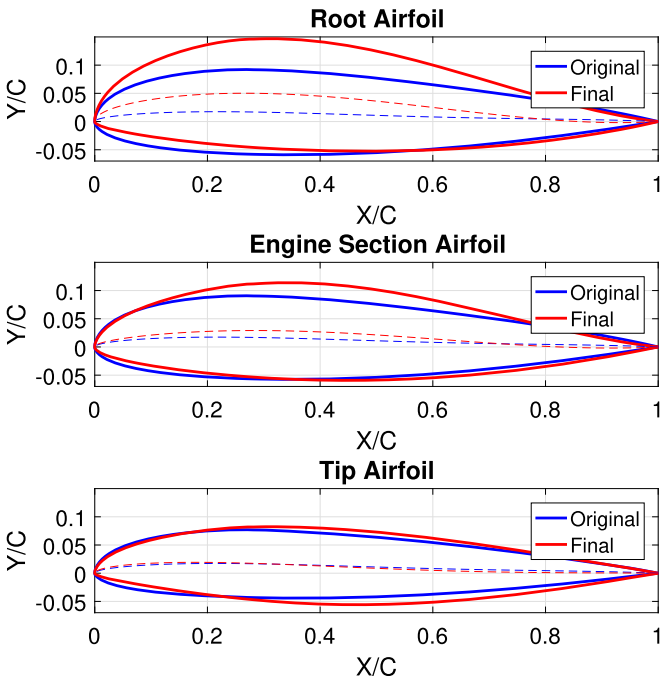

Fig. 17. Optimal airfoils searching RBF.

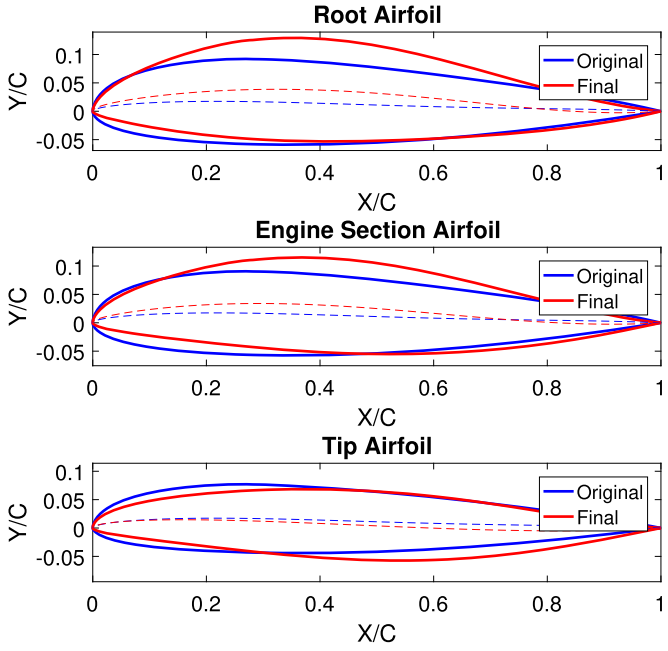

Fig. 18. Optimal airfoils Searching Kriging.

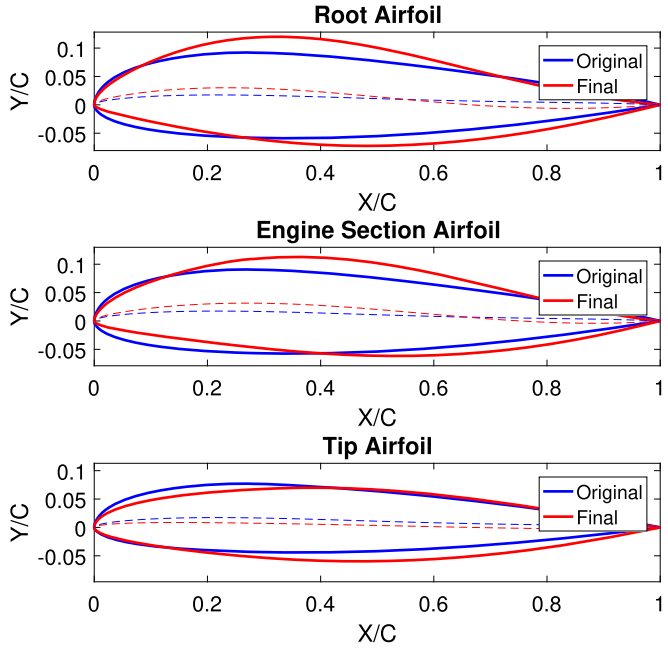

Fig. 19. Optimal airfoils EGO.

consideration of wing–propeller interactions. The research objective was to build appropriate analysis tools to model the most relevant effects of the aerodynamic interaction, integrate the tools into an MDA, and develop suitable optimization architectures enhanced by surrogate models. In this research, new physics-based and semi-empirical approaches to perform a *full interaction* analysis of wing–propeller aerodynamics were developed, including routines to model propeller streamtube deflection and wing swirl recovery.

The results make it possible to draw some important conclusions about the implementation of surrogate based local optimization frameworks for our problem of wing design with propeller–wing interaction. First, satisfactory performance can only be achieved by a combination of two factors, namely suitable surrogate models and the generation of a DOE with sufficiently wide bounds. RBF models were shown to be not well suited to the problem, as reflected both by the rather poor fuel weight error metrics and by the optima achieved in the frameworks using RBF models. Kriging models, however, demonstrated a very high accuracy, and both Kriging based SQP searching surrogate models and the EGO approach resulted in better optimum points.

It should be concluded that satisfactory results with surrogate based optimization can only be obtained with a design of experiments with adequate sampling density and bounds and with suitable surrogate models available at the beginning of the optimization process. In this respect, radial basis function surrogates

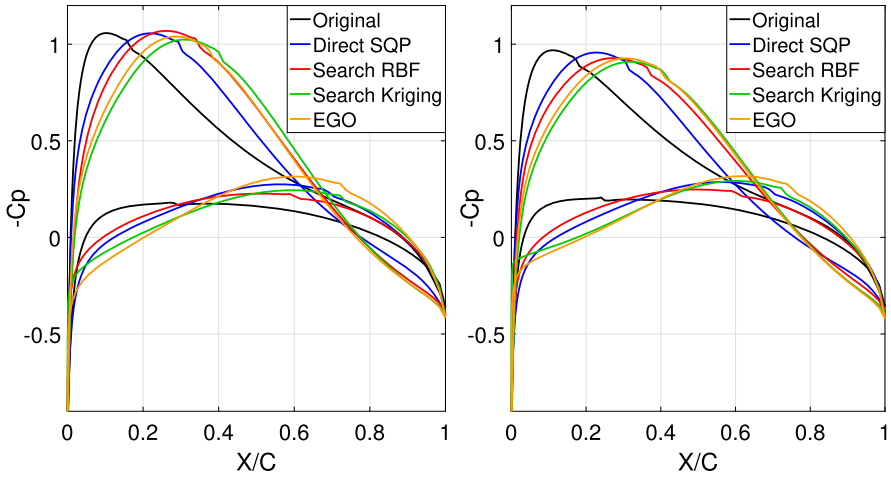

Fig. 20. Optimal designs' pressure coefficient distributions at two significant slipstream blown sections: 0.45 m inboard (left figure) and 0.45 m outboard (right figure) of propeller axis.

were deemed less suitable for our problem in comparison to other surrogate model types, and, in particular, for capturing the effects of airfoil CST shape parameters. Conversely, surrogate validation and the optimization results demonstrated that Kriging resulted in the greatest accuracy and suitability for our analysis. The implementation of a strategy for infrequent updating of Kriging hyperparameters was also shown to considerably limit time costs while retaining satisfactory accuracy.

The EGO approach was found to demonstrate satisfactory performance when compared to a direct global optimization. In the context of the present analysis, in which limited multi-modal behavior was observed, the Kriging-based searching surrogate models framework performing a local search was deemed the most preferable approach, both in terms of objective function improvement and in terms of computational time required.

Conflict of interest statement

None declared.

References

[1] M. Moore, K. Goodrich, J. Viken, J. Smith, B. Fredericks, T. Trani, J. Barraclough, B. German, M. Patterson, High-speed mobility through on-demand aviation, in: 2013 Aviation Technology, Integration, and Operations Conference, 2013.
[2] L.L.M. Veldhuis, Review of propeller–wing aerodynamic interference, in: 24th International Congress of the Aeronautical Sciences, 2004.
[3] F.M. Catalano, On the effects of an installed propeller slipstream on wing aerodynamic characteristics, Acta Polytech. 44 (3) (2004).
[4] L.L.M. Veldhuis, Propeller Wing Aerodynamic Interference, Delft University of Technology, 2005.
[5] D.P. Witkowski, A.K.H. Lee, J.P. Sullivan, Aerodynamic interaction between propellers and wings, J. Aircr. 26 (9) (1989) 829–836.
[6] J. Cho, J. Cho, Quasi-steady aerodynamic analysis of propeller–wing interaction, Int. J. Numer. Methods Fluids 30 (1999) 1027–1042, https://doi.org/10.1002/(SICI)1097-0363(19990830)30:83.0.CO;2-R.
[7] G. Ferraro, T. Kipouros, A.M. Savill, A. Rampurawala, C. Agostinelli, Propeller–wing interaction prediction for early design, in: AIAA SciTech: Science and Technology Forum and Exposition, National Harbor, Maryland, 2014.
[8] M.D. Patterson, M.J. Daskilewicz, B.J. German, Conceptual design of electric aircraft with distributed propellers: multidisciplinary analysis needs and aerodynamic modeling development, in: Proceedings of the 52nd AIAA Aerospace Sciences Meeting, 2014, 2014-0534.
[9] M.D. Patterson, B.J. German, Wing aerodynamic analysis incorporating one-way interaction with distributed propellers, in: 14th AIAA Aviation Technology, Integration, and Operations Conference, Atlanta, GA, USA, 2014.
[10] M. Drela, H. Youngren, XROTOR Download Page, 2011.
[11] S. Goldstein, On the vortex theory of screw propellers, Proc. R. Soc. Lond., a Contain. Pap. Math. Phys. Character 123 (792) (1929) 440–465, https://doi.org/10.1098/rspa.1929.0078.
[12] J.T. Conway, Analytical solutions for the actuator disk with variable radial distribution of load, J. Fluid Mech. 297 (1995) 327–355, https://doi.org/10.1017/S0022112095003120.
[13] J. De Young, Propeller at high incidence, J. Aircr. 2 (3) (1965) 241–250, https://doi.org/10.2514/3.43646.
[14] H.S. Ribner, Formulas for Propellers in Yaw and Charts of the Side-Force Derivative, NACA Technical Report N.819, 1945.
[15] H.S. Ribner, Propellers in Yaw, NACA Technical Report 820, 1945.
[16] J. Katz, A. Plotkin, Low-Speed Aerodynamics, Cambridge University Press, Cambridge, UK, 2001, p. 613.
[17] T. Melin, User's Guide and Reference Manual for Tornado, Royal Inst. of Technology (KTH), Stockholm, Sweden, 2000.
[18] J. Mariens, A. Elham, M.J.L. van Tooren, Quasi-three-dimensional aerodynamic solver for multidisciplinary design optimization of lifting surfaces, J. Aircr. 51 (2) (2014) 547–558, https://doi.org/10.2514/1.C032261.
[19] M. Drela, H. Youngren, XFOIL: subsonic airfoil development system, software package, available online at http://web.mit.edu/drela/Public/web/xfoil, 2004 [retrieved Feb. 2011].
[20] L. Ting, C.H. Liu, G. Kleinstein, Interference of wing and multi-propellers, AIAA J. 10 (7) (1971) 906–914, https://doi.org/10.2514/3.50244.
[21] I. Samuelsson, Low speed wind tunnel investigation of propeller slipstream aerodynamic effects on different nacelle/wing combinations, in: ICAS, 16 th Congress, Jerusalem, Israel, 1988, pp. 1749–1765.
[22] I. Kroo, R. Shevell, Aircraft Design: Synthesis and Analysis, Desktop Aeronautics Inc., 2001, Textbook Version 0.99.
[23] A. Elham, G. La Rocca, M.J.L. Van Tooren, Development and implementation of an advanced, design-sensitive method for wing weight estimation, Aerosp. Sci. Technol. 29 (1) (2013) 100–113.
[24] https://www.tecnam.com/aircraft/p2012-traveller.
[25] B.M. Kulfan, Universal parametric geometry representation method, J. Aircr. 29 (1) (2008) 142–158, https://doi.org/10.2514/1.29958.
[26] I. Couckuyt, T. Dhaene, P. Demeester, ooDACE toolbox: a flexible object-oriented Kriging implementation, J. Mach. Learn. Res. 15 (1) (2014) 3183–3186.
[27] S. Koziel, D. Echeverría Ciaurri, Leifur Leifsson, Surrogate-based methods, in: Computational Optimization, Methods and Algorithms, 2011, pp. 33–59.
[28] G.G. Wang, S. Shan, Review of metamodeling techniques in support of engineering design optimization, J. Mech. Des. 129 (4) (2007) 370–380, https://doi.org/10.1115/1.2429697.
[29] D.R. Jones, M. Schonlau, W.J. Welch, Efficient global optimization of expensive black-box functions, J. Glob. Optim. 13 (4) (1998) 455–492.
[30] P. Refaeilzadeh, L. Tang, H. Liu, Cross-validation, in: Encyclopedia of Database Systems, 2009, pp. 532–538.
[31] M.Y.M. Ahmed, N. Qin, Surrogate-based aerodynamics design optimization: use of surrogates in aerodynamics design optimization, in: 13th International Conference on Aerospace Science & Aviation Technology, Cairo, Egypt, 2009, pp. 26–28.
[32] Z.-H. Han, K.-S. Zhang, Surrogate-Based Optimization, INTECH Open Access Publisher, 2012.
[33] A. Keane, P. Nair, Computational Approaches for Aerospace Design: The Pursuit of Excellence, John Wiley & Sons, 2005.
[34] A.I.J. Forrester, A.J. Keane, Recent advances in surrogate-based optimization, Prog. Aerosp. Sci. 45 (1) (2009) 50–79, https://doi.org/10.1016/j.paerosci.2008.11.001.
[35] J.R.R.A. Martins, A.B. Lambe, Multidisciplinary design optimization: a survey of architectures, AIAA J. 51 (1) (2013) 2049–2075, https://doi.org/10.2514/1.J051895.